Dual-Band Coherent Microwave Photonic Radar Using Linear Frequency Modulated Signals With Arbitrary Chirp Rates

Xiangchuan Wang , Fengting Cao, Cong Ma , Yue Yang, Fangzheng Zhang , *Senior Member, IEEE*, and Shilong Pan , *Fellow, IEEE*

(Invited Paper)

Abstract—**Multi-band radars can obtain more electromagnetic scattering information of targets in complex electromagnetic environments, but they always suffer from complex configurations, small bandwidth, or fixed waveforms. Here, we propose a dual-band coherent microwave photonic radar, which is simple, reconfigurable, and has a wide operational bandwidth. In the proposed system, dual-band linear frequency modulated (LFM) signals with arbitrary chirp rates and adjustable bandwidths are simultaneously generated based on polarization multiplexing, and de-chirp processed using photonic in-phase and quadrature (I/Q) mixing. By fusing the de-chirped signals, ranging and inverse synthetic aperture radar (ISAR) imaging with a resolution that is proportional to the sum of the instantaneous bandwidths of the two bands is realized. In an experiment, the dual-band microwave photonic radar is built to generate and process dual-band LFM signals with different instantaneous bandwidths and chirp rates covering 18.1–23.1 GHz and 22.9–29.9 GHz. De-chirped signals in the two bands are coherently fused, achieving an equivalent bandwidth of 11.8 GHz and a range resolution of 1.31 cm.**

Index Terms—**Dual-band radar, high range resolution, ISAR, microwave photonics.**

I. INTRODUCTION

HIGH-RESOLUTION detection of complex targets is critical to modern radars for applications such as small uncrewed aerial vehicle (UAV) tracking, intelligent driving, and multi-target imaging [1]. In contrast to single-band radars, dual-band radars can obtain electromagnetic scattering information in different frequency bands, which can provide more target information and is of great importance in target recognition [2], [3]. Dual-band radars also provide better anti-interference performance than single-band radars so that they can obtain more reliable detection in complex electromagnetic environments. Furthermore, a dual-band radar system supports the fusion of received signals in two different bands, which could dramatically improve the resolution of detection [4], [5]. Lincoln Laboratory conducted early research on multi-band fusion radar imaging. They completed the experiment of distinguishing different scatterers of a reentry vehicle model after coherently combining two sparse subbands [6]. However, traditional dual-band radar systems usually consist of two independent radars, significantly increasing the cost and complexity. A complex compensation algorithm should also be applied to deal with the incoherence of the dual-band signals induced by vibrational time delay and phase difference between the two radars [7], [8]. In addition, conventional electronic radar systems suffer from limited bandwidth, so generating and processing dual-band radar signals with high-frequency and large bandwidths are difficult.

Microwave photonics features large instantaneous bandwidth, parallel signal processing, and multi-dimensional multiplexing, which is promising for implementing multi-band high-resolution radars [9], [10], [11], [12]. Much research has been conducted on generating and processing multi-band signals based on microwave photonic technologies. Previously, microwave photonic frequency multiplying combined with polarization multiplexing has been used to generate dual-band waveforms [13], [14], [15]. By applying two different radio frequency (RF) signals and a coding signal to a dual-polarization dual-parallel Mach-Zehnder modulator (DP-DPMZM), a dual-band dual-chirp microwave signal in the C and X bands is generated [15]. Other photonic methods based on optical frequency combs, optoelectronic oscillators, and optical injection in semiconductor lasers are also proposed to generate multi-band signals [16], [17], [18], [19], showing significant advantages in instantaneous bandwidth and reconfigurability.

By applying these multi-band signals to radars, the system performance, such as reconfigurability, range resolution, and recognition accuracy, can be greatly enhanced [20], [21], [22], [23], [24], [25], [26]. However, for multi-band radars, it is a significant challenge to distinguish the echoes in different

bands. A common approach is using electrical band-pass filters (EBPFs) to select signals in the corresponding frequency band and perform subsequent signal processing. For example, a photonics-based multi-band radar operating in the S and X bands has been investigated [22], where two signals, each having a bandwidth of 18 MHz, are produced in the transmitter and separated by two EBPFs in the receiver. The range resolution was doubled by data fusion, equivalent to the case with a bandwidth of 36 MHz. Similarly, two EBPFs are used to separate the echoes of two bands in a dual-band radar based on a photonic digital-to-analog converter [24]. However, it is impossible to separate the echoes using EBPFs when the signals in two bands have similar or overlapping frequencies. To avoid the use of EBPFs, in a frequency-to-time mapping (FTM) based dual-band radar system [25], terahertz signals in two bands are distinguished by down-converting them into the same baseband at different time slots. Nevertheless, the time-division multiplexing method causes low detection efficiency. Using a microwave photonic receiver based on a dual-polarization quadrature phase shift keying modulator [26] to receive the dual-band signals simultaneously, the detection efficiency is improved while the structure is simplified. However, the system is only effective when the linear frequency modulated (LFM) signals have different chirp rates. If the chirp rates are equal, the de-chirped signals will be the same, and the system would fail to work. It should be noted that in-phase and quadrature (I/Q) demodulation is usually required to avoid the mirror image of the target in de-chirp receivers. In [27], a microwave photonic I/Q receiver with high image rejection has been proposed to demodulate a dual-band signal, but it can only handle two LFM signals with exactly opposite chirp rates, limiting the radar's capability to process reconfigurable LFM signals.

In this paper, we propose and demonstrate a wideband and reconfigurable dual-band microwave photonic radar. In the transmitter, dual-band coherent LFM signals with arbitrary chirp rates and adjustable bandwidths are simultaneously generated based on polarization multiplexing. In the receiver, I/Q de-chirping of the reconfigurable dual-band LFM signals is performed. Based on the multiplexed microwave photonic link, signals de-chirped from the two bands are coherent. Therefore, they can be further fused to achieve larger synthetic bandwidth. Different from our previous work [28], where a ranging radar using dual-band LFM signals with the same chirp rate has been demonstrated, high-resolution ranging and inverse synthetic aperture radar (ISAR) imaging has been performed using signals with variable chirp rates.

II. PRINCIPLE

The schematic diagram of the proposed dual-band coherent microwave photonic radar is depicted in Fig. 1. An optical carrier with a center frequency of f_0 is modulated by two LFM signals via a dual-polarization Mach-Zehnder modulator (Dpol-MZM). The modulator comprises a 3-dB coupler, two Mach-Zehnder modulators (MZMs), and a polarization rotator (PR) followed by a polarization beam combiner. The two LFM microwave signals can be written as $V_i(t) = V_m\cos(2\pi f_i t + \pi k_i t^2)$, where k_i
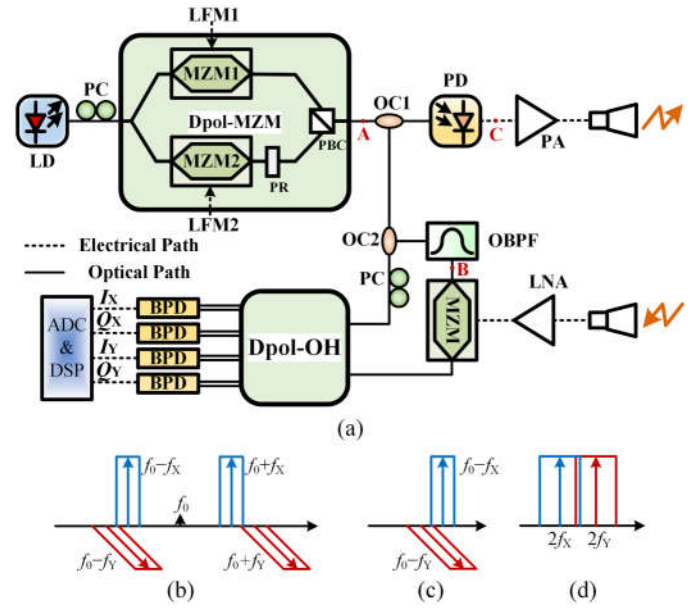

Fig. 1. (a) Schematic of the dual-band coherent microwave photonic radar. LD, laser diode; PC, polarization controller; MZM, Mach-Zehnder modulator; Dpol-MZM, dual polarization MZM; PR, polarization rotator; PBC, polarization beam combiner; OC, optical coupler; PD, photodetector; OBPF, optical bandpass filter; PA: Power amplifier; LNA, low noise amplifier; Dpol-OH, dual polarization optical hybrid; BPD, balanced photodetector; ADC, analog to digital converter; DSP, digital signal processor. (b) Optical spectrum output from the Dpol-MZM at point A. (c) Optical spectrum output from the OBPF at point B. (d) Electrical spectrum of dual-band microwave signals generated by the PD at point C.

is the chirp rate, f_i is the center frequency, V_m is the amplitude, and i represents the X and Y polarization. One LFM signal is applied to the X-polarization modulator of the Dpol-MZM, while the other is applied to the Y-polarization modulator. Both modulators operate in the carrier-suppressed double-sideband modulation mode. The modulated optical signals output from the Dpol-MZM can be expressed as

$$E_i(t) \propto J_1(\beta)e^{j2\pi f_0 t}\left[e^{j\left(2\pi f_i t + \pi k_i t^2\right)} + e^{-j\left(2\pi f_i t + \pi k_i t^2\right)}\right] \tag{1}$$

where J_1 is the 1st-order Bessel function of the first kind, $\beta = V_m/2V_\pi$ is the modulation index, and V_π is the half-wave voltage of the modulator. $E_Y(t)$ is obtained after passing through the PR, which is perpendicular to the polarization direction of $E_X(t)$. The optical polarization-multiplexed signal composed of $E_X(t)$ and $E_Y(t)$ is divided into two branches after an optical coupler (OC). The upper branch is photoelectrically converted in a photodetector (PD). Thus dual-band microwave signals are obtained, given by

$$P(t) \propto \sum_{i=1}^{2}\cos[2(2\pi f_i t + \pi k_i t^2)] \tag{2}$$

In addition, the above operation realizes frequency doubling of the input microwave signal. The lower branch out of OC1 is sent to the receiver as an optical reference and further divided

into two branches by OC2. The left branch is sent to a dual polarization optical hybrid (Dpol-OH) integrating two 90° optical hybrids. The right branch is fed into an MZM after selecting one sideband by an optical bandpass filter (OBPF) and modulated by the echo signal. It is assumed that the delay between the echo signal and the transmitted signal is τ. The signal output from the MZM biased at the minimum transmission point is expressed as

$$E_S(t) \propto e^{j2\pi[f_0-f_X-k_Xt]t}$$

$$\cos\left(4\pi f_X(t-\tau)+2\pi k_X(t-\tau)^2\right)$$

$$+ e^{j2\pi[f_0-f_X-k_Xt]t}\cos\left(4\pi f_Y(t-\tau)+2\pi k_Y(t-\tau)^2\right)$$

$$+ e^{j2\pi[f_0-f_Y-k_Yt]t}\cos\left(4\pi f_X(t-\tau)+2\pi k_X(t-\tau)^2\right)$$

$$+ e^{j2\pi[f_0-f_Y-k_Yt]t}\cos\left(4\pi f_Y(t-\tau)+2\pi k_Y(t-\tau)^2\right) \quad (3)$$

The modulated optical signal is sent to the Dpol-OH, where four 90° phase-stepped interferences are performed with the optical reference signal in the two polarizations.

The eight output signals are sent into four balanced photodetectors (BPDs) for balanced photodetection, generating two groups of de-chirped signals, given by

$$\begin{bmatrix} I_i(t) \\ Q_i(t) \end{bmatrix} \propto \begin{bmatrix} \cos\left[2\pi\left(2k_i\tau t - k_i\tau^2 + 2f_i\tau\right)\right] \\ \sin\left[2\pi\left(2k_i\tau t - k_i\tau^2 + 2f_i\tau\right)\right] \end{bmatrix} \quad (4)$$

By effectively utilizing the signals in (4), the operation bandwidth can be expanded. $k_i\tau^2$ is the residual video phase (RVP), which can be ignored in the fusion process. When the chirp rates of the two band signals are the same, i.e., $k_X = k_Y$, the two sets of signals $I_X(t)$ and $I_Y(t)$ or $Q_X(t)$ and $Q_Y(t)$ can be spliced into one continuous signal in the time domain by directly time-shift processing and discarding the duplicates. For example, if the coherent de-chirped signal $I_X(t)$ and $I_Y(t)$ are synthesized, $I_Y(t)$ should be time-shifted by $(f_Y-f_X)/k_X$. The signal $I_X(t)$ and $I_Y(t)$ are expressed as

$$\begin{bmatrix} I_X(t) \\ I_Y(t) \end{bmatrix} \propto \begin{bmatrix} \cos\left[2\pi\left(2k_X\tau t - k_X\tau^2 + 2f_X\tau\right)\right] \\ \cos\left[2\pi\left(2k_Y\tau t - k_Y\tau^2 + 2f_Y\tau\right)\right] \end{bmatrix} \quad (5)$$

and $I_Y(t-(f_Y-f_X)/k_X)$ is given by

$$I_Y\left(t - \frac{f_Y-f_X}{k_X}\right)$$

$$= \cos\left[2\pi\left(2k_Y\tau\left(t - \frac{f_Y-f_X}{k_X}\right) - k_Y\tau^2 + 2f_Y\tau\right)\right]$$

$$= \cos\left[2\pi\left(2k_X\tau\left(t - \frac{f_Y-f_X}{k_X}\right) - k_X\tau^2 + 2f_X\tau\right)\right]$$

$$= \cos\left[2\pi\left(2k_X\tau t - k_X\tau^2 + 2f_X\tau\right)\right] \quad (6)$$

Thus, $I_X(t)$ and $I_Y(t)$ can be synthesized [5].

When the chirp rates are different, the fractional sampling rate conversion must first be performed to correct the frequencies of the de-chirped signals in the two bands [29]. There is a definite relationship between the de-chirped frequency and the chirp rate of the two bands, i.e., $f_X/f_Y = k_X/k_Y$. Taking one of the de-chirped signals as a reference, the other de-chirped signal is
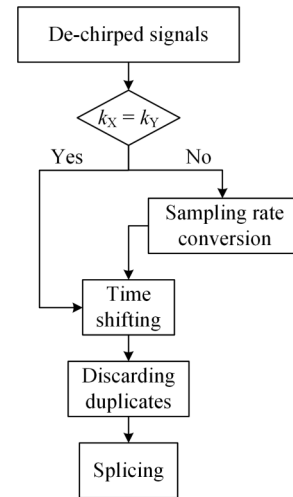

Fig. 2. Schematic flow chart of coherent fusion of the de-chirped signals.

interpolated or extracted for frequency correction according to the relationship. The processed signal has a new sequence length, in effect corresponding to a new sampling rate. This treatment is equivalent to the fractional sampling rate conversion. After the frequencies of the two de-chirped signals are processed to be consistent with each other, the signal synthesis can be performed by the above processing method. The synthesis of the quadrature signals $Q_X(t)$ and $Q_Y(t)$ can be performed in the same way as the synthesis of the de-chirped signals $I_X(t)$ and $I_Y(t)$. $I_X(t)$ and $I_Y(t)$ are synthesized to obtain the signal $I(t)$, while $Q_X(t)$ and $Q_Y(t)$ are synthesized to obtain the signal $Q(t)$. Finally, a complex signal $s(t) = I(t)+jQ(t)$ is obtained.

Then, the target can be located after a fast Fourier transform (FFT) is performed on the complex signal to analyze the frequency of the spectrum. A simple schematic flow chart of the processing is displayed in Fig. 2. To facilitate signal synthesis or fusion, the frequency ranges of the two bands need to be continuous or have a small overlap, i.e., $f_Y-f_X \leq 1/2/(B_X+B_Y)$, where B_i is the bandwidth of LFM signals in different bands. In this case, complex algorithms do not need to be used to restore the frequency vacancy. After synthesis, the equivalent bandwidth of the system is expanded.

It should be noted that when the chirp rates of signals in two bands are different, the phase difference of the two de-chirped signals introduced by RVP may be large enough to affect the fusion of the de-chirped signals. Reference signal in the system is transmitted through optical fibers, and the reference delay is controlled by adjusting the length of optical fibers or using controllable optical fiber delay lines. Since a delay of τ_{ref} can be added to the reference signal in the proposed system, the de-chirped signal can be represented as

$$r_i(t) \propto \cos$$

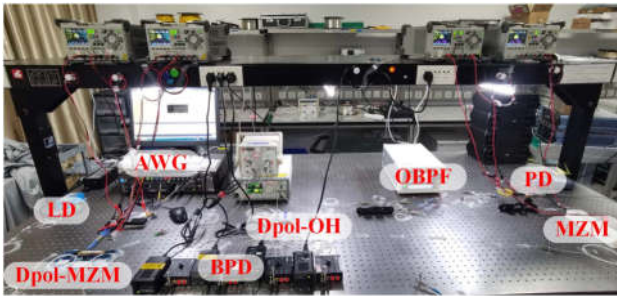$$\left[2\pi k_i|\tau-\tau_{ref}|t + 2\pi f_i|\tau-\tau_{ref}| - \pi k_i\left(\tau^2-\tau_{ref}^2\right)\right] \quad (7)$$

Fig. 3. Picture of the experimental setup.

Fig. 4. Time-frequency diagrams of the LFM signals with the same chirp rate along (a) the X polarization and (b) the Y polarization.

By changing τ_{ref} to minimize the relative delay between the reference delay τ_{ref} and the target echo delay τ, the RVP will be as small as possible, which is conducive to phase correction.

III. EXPERIMENT AND DISCUSSION

Experiments based on dual-band LFM signals with the same and different chirp rates have been carried out to verify the feasibility of the proposed method. The picture of the experimental setup is shown in Fig. 3. A narrow linewidth laser (Teraxion PS-NLL) emits an optical carrier with a wavelength of about 1550.12 nm, and is then divided into two paths in the built-in coupler of the Dpol-MZM (FTM7980). Two LFM signals generated by an arbitrary waveform generator (AWG, Keysight M9502A) are fed into the two MZMs in the X and Y polarizations of the Dpol-MZM to modulate the optical carrier.

Carrier-suppressed double-sideband modulated optical signals along the orthogonal polarizations are generated and then divided into two paths by OC1. The upper path performs photoelectric conversion in a 40-GHz PD (Finisar XPDV2120R), in which the optical signals along the two polarizations beat, respectively. Thus dual-band microwave signals with doubled frequency and bandwidth are obtained simultaneously and transmitted to the free space by a double-ridged horn antenna after being amplified. The lower one, as the reference signal of the receiver, is further divided into two paths by OC2. One sideband of the carrier-suppressed optical double-sideband modulated signal is filtered out by an OBPF (Santec OTF-980), to serve as the optical carrier to the MZM in the receiver. The two-polarization sidebands are jointly projected to the modulation axis of the MZM with the same power.

Echoes from the targets are collected by the receiving antenna and used to drive the MZM (Fujitsu FTM7938) after being amplified by a low-noise amplifier (LNA). The echo-modulated optical signal is sent to the optical hybrid. The optical reference signals along the two polarizations are split by a polarization beam splitter (PBS) integrated in the Dpol-OH (Kylia COH28). Afterward, interferences between each split signal and the echo-modulated optical signal are done in the two integrated optical hybrids. Each pair of signals in the outputs of the Dpol-OH enters a BPD (Thorlabs PDB450C) for balanced detection. Finally, de-chirped signals of the two frequency bands are obtained along the X and Y polarizations, respectively.
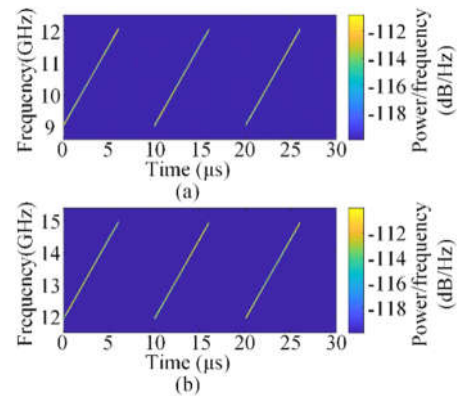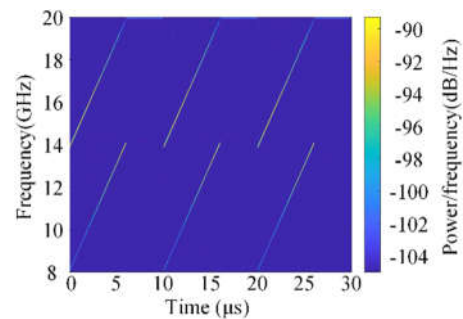

Fig. 5. Time-frequency diagram of the down-converted transmitted signal.

First, the AWG generates LFM signals with a bandwidth of 3 GHz, a pulse width of 6 μs, and a period of 10 μs, centered at 10.55 GHz and 13.45 GHz, respectively. The time-frequency diagram of the generated signals is shown in Fig. 4. The chirp rates k_{X} and k_{Y} are 0.5×10^{15} Hz/s. The center frequencies of the generated signals in the two bands are 21.1 GHz and 26.9 GHz, respectively, while their bandwidths are both 6 GHz. In the experiment, the radar signals are down-converted with a 10-GHz signal to analyze its time-frequency relationship due to the bandwidth limitation of the oscilloscope. The time-frequency diagram of the down-converted radar signal is shown in Fig. 5. As can be seen, signals with frequencies of 18.1–24.1 GHz (Band 1) and 23.9–29.9 GHz (Band 2) are generated simultaneously. The frequency and bandwidth of the RF signals are doubled compared with the input LFM signals.

The pulse width and bandwidth are broadened to 11.8 μs and 11.8 GHz after two signals with 0.2 GHz overlap are synthesized. The equivalent operating frequency covers from 18.1 to 29.9 GHz. Fig. 6 shows the spectra of the synthetic and single-band de-chirped signal for single-target ranging. The ranging results based on the synthesis and two single bands are about 1.227 m, 1.222 m, and 1.227 m, respectively, calculated by the peak frequencies of 8.178 MHz, 8.148 MHz, and 8.181 MHz. The ranging error after signal synthesis is within the subcentimeter level. For LFM radars, the range resolution can be estimated by the 3 dB bandwidth of the lobe [30], [31]. The 3 dB bandwidth of the main lobe given by band 1, band 2, and the fused signal
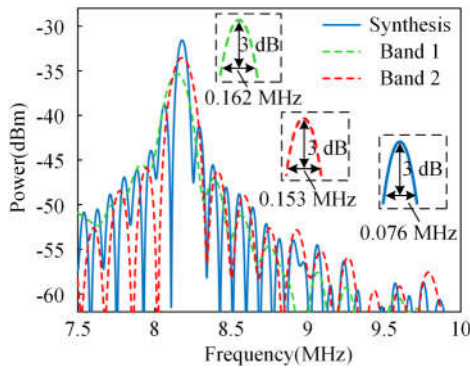
Fig. 6. Spectra of the synthetic and single-band de-chirped signal under single-target ranging. Band 1 covers 18.1–24.1 GHz, and Band 2 covers 23.9–29.9 GHz.
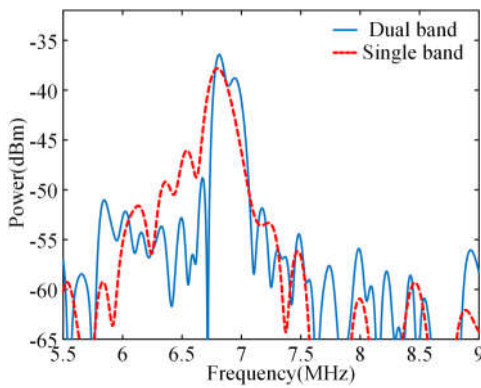

Fig. 7. Spectra of the complex signals de-chirped from dual-band and single-band LFM signals when two targets are placed at a distance of 1.8 cm.
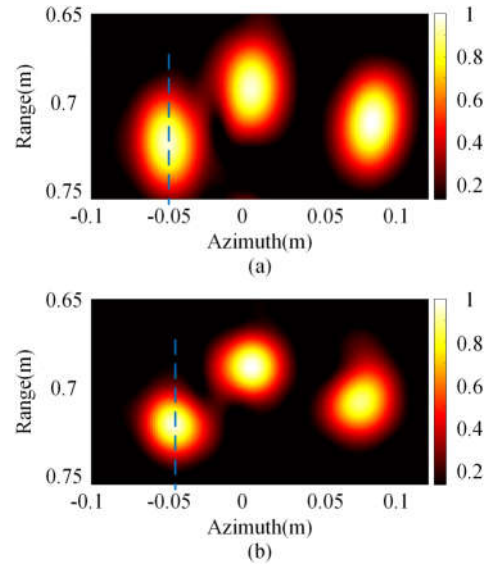

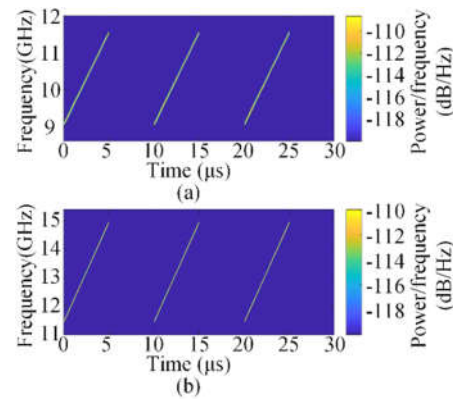Fig. 8. ISAR image based on (a) single-band detection and (b) dual-band fusion.

Fig. 9. Time-frequency diagrams of the LFM signals with different chirp rates loading along (a) the X polarization and (b) the Y polarization.

from the zoomed-in view is 162 kHz, 153 kHz, and 76 kHz. The calculated range resolutions are 2.43 cm, 2.3 cm, and 1.14 cm, respectively. With the increase of equivalent bandwidth, 3 dB bandwidth narrows and range resolution improves. The power difference between the two peaks of the spectra based on the single-band signal is compensated in the synthesis. It can be found that the power of the synthesized signal is increased due to the coherent signal fusion. The improvement of the system resolution is also verified in a two-target detection experiment. Fig. 7 shows the spectra of the complex signals de-chirped from the dual-band and single-band LFM signals when two targets are placed with a distance of 1.8 cm. The two targets can be easily distinguished by the synthesized de-chirped signal (the solid blue line), but cannot be determined by the single-band de-chirped signal (the dashed red line). The detected target spacing is 1.86 cm after synthesis, which is close to the set value.

Next, the imaging performance of the system is investigated. Three corner reflectors are placed on a turntable rotating at 720 degrees per second. The set imaging angle range is 20 degrees. The ISAR image using a single-band signal is shown in Fig. 8(a), and that by dual-band fusion is given in Fig. 8(b). After data fusion, the images of the three targets narrow in range as compared with the range-resolved profile along the dashed blue line,

showing that the dual-band fusion method improves the range resolution of ISAR imaging.

As discussed in Section II, the proposed dual-band radar in Fig. 1 can generate two high-frequency and large-bandwidth LFM signals with arbitrary chirp rates, featuring anti-interference capability. Here, the AWG generates LFM signals with a pulse width of 5 μs and a period of 10 μs, centered at 10.3 GHz and 13.2 GHz, respectively. The bandwidths are 2.5 GHz and 3.5 GHz. The time-frequency diagram is given in Fig. 9. The chirp rate k_X is 0.5×10^{15} Hz/s while k_Y is 0.7×10^{15} Hz/s. After photonic frequency doubling, the center frequencies of the transmitted signals are 20.6 GHz and 26.4 GHz, and the bandwidths are 5 GHz and 7 GHz, respectively. Similarly, a 10-GHz single-frequency signal is used to down-converted the transmitted radar signal in the experiment so that the oscilloscope can record the high-frequency signals. Fig. 10 depicts the time-frequency diagram of the down-converted signal. It can be confirmed that the radar system operates in the frequency
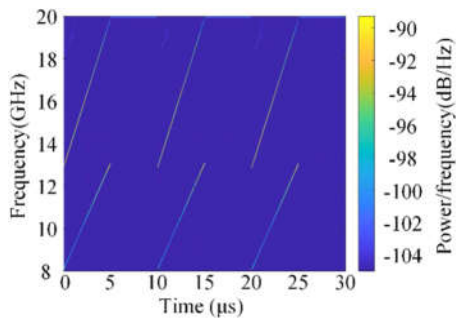
Fig. 10. Time-frequency diagram of the down-converted transmitted radar signal.
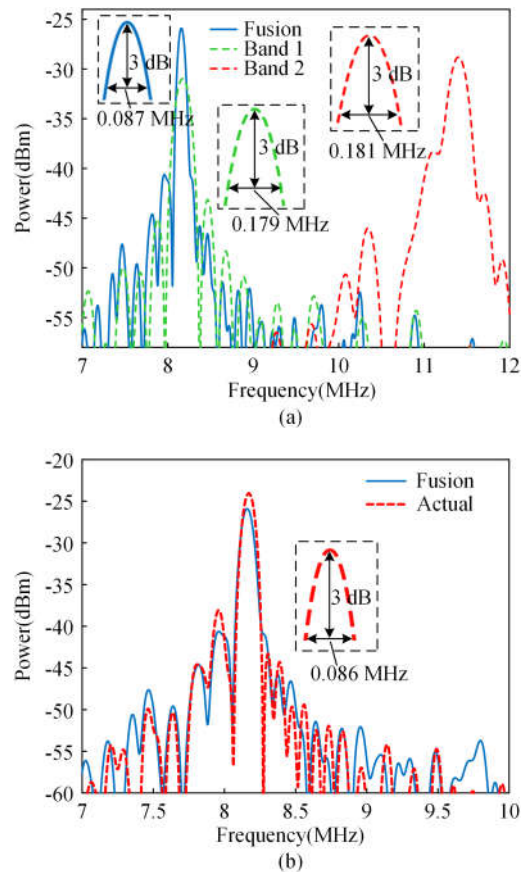

Fig. 11. (a) Spectra of the de-chirped signal with single-band detection and dual-band fusion for single-target ranging. (b) Spectra of the fused and actual wideband de-chirped signal for single-target detection. Band 1 covers 18.1–23.1 GHz, and Band 2 covers 22.9–29.9 GHz.

range of 18.1–23.1 GHz (Band 1) and 22.9–29.9 GHz (Band 2), simultaneously.

Because of the different chirp rates, there is a difference between the center frequencies of the de-chirped signals. Therefore, the de-chirped signals cannot be simply synthesized as those in the aforementioned experiments, and a frequency correction should be performed. To do so, the frequency of the de-chirped signal in Band 1 is used as a reference to calibrate the frequency of the de-chirped signal in Band 2 according to the relationship between the frequency and chirp rate of the two signals. The de-chirped signal of Band 2 is interpolated to achieve the fractional sampling rate conversion. Then, the frequency of Band 2 is equal to that of Band 1, so the synthesis algorithm can be used to fuse the signals in the two bands. The bandwidths of the transmitted signals in Band 1 and Band 2 are 5 GHz and 7 GHz, respectively, while the bandwidth of the fused signal is 11.8 GHz. Experimental results based on single-band detection, dual-band fusion, and an actual wideband signal with the equivalent operating frequency range (18.1 GHz–29.9 GHz) are analyzed. In the comparative investigation, the experimental equipment and structure of the aforementioned experiments are used.

After performing FFT on the de-chirped signals and correcting the reference delay in the link, the spectrograms shown in Fig. 11(a) are obtained. The peak in the spectrum of the de-chirped signal in Band 1 is located at 8.174 MHz, corresponding to the target position of 1.226 m. The spectrum of the de-chirped signal in Band 2 presents a peak frequency of 11.4 MHz, which is 1.4 times that of the de-chirped signal in Band 1 because the chirp rate of the signal in Band 2 is 1.4 times that of the signal in Band 1. The calculated distance of the target is 1.221 m. The solid blue line results from the fusion of the signals in the two bands, showing a peak frequency of 8.16 MHz, which corresponds to a target distance of 1.224 m. The 3 dB bandwidth of the main lobe given by the fused signal from the zoomed-in view is 87.5 kHz, which is significantly smaller than that of the other two curves. According to the figures, the range resolutions for the systems using the signals in Band 1, Band 2, and both bands are 2.7 cm, 1.94 cm, and 1.31 cm, respectively. In Fig. 11(b), the spectra obtained by the fusion of the signals in the two bands (the solid blue line) and by the actual wideband signal (the dashed red line) are compared. The

center frequency in the dashed red line is found to be 8.17 MHz, and the calculated target distance is 1.226 m. The consistency between the fused and actual detection verifies the feasibility of the coherent fusion method for signals in different frequency bands.

In addition, several sets of experiments have also been carried out to validate the fusion method, such as the two-target detection experiment when the two targets are separated by 1.8 cm. It is apparent from Fig. 12 that the fused signal detection system can discriminate the two targets, whereas the relatively large bandwidth of the 7-GHz single-band signal cannot distinguish them. The frequencies of the two peaks in the spectra are found to be 6.754 MHz and 6.877 MHz, corresponding to the calculated target spacing of 1.845 cm with a measurement error of 0.045 cm.

The proposed system is also capable of performing ISAR imaging. The rotation speed of the turntable where the targets are placed is set to 720 degrees per second. The imaging angle range is 15 degrees. A picture of "V" consisting of five corner reflectors is shown in Fig. 13(a). The ISAR image of the target "V" detected by Band 1 and Band 2 are shown in Fig. 13(b) and (c), respectively. Fig. 13(d) shows the imaging result of the dual-band fusion. With the increase of the equivalent detection
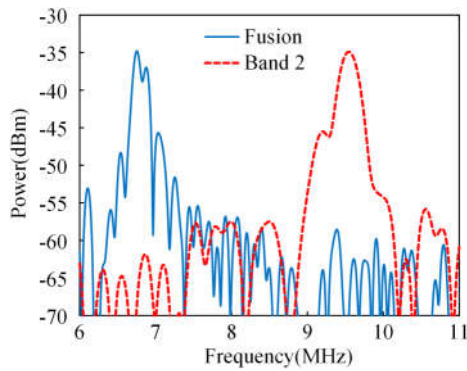
Fig. 12. Spectra of the fused dual-band signal with an equivalent bandwidth of 11.8 GHz and a single-band signal with a bandwidth of 7 GHz when two targets are separated by 1.8 cm.
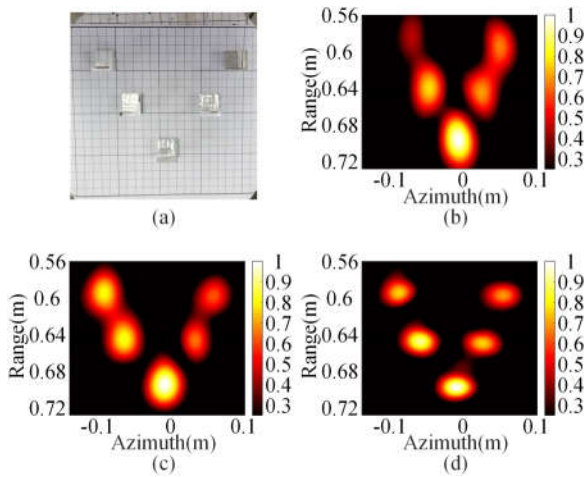

Fig. 13. Picture of (a) target and ISAR image detected by (b) 5 GHz signal in Band 1, (c) 7 GHz signal in Band 2, and (d) 11.8 GHz signal after fusion.
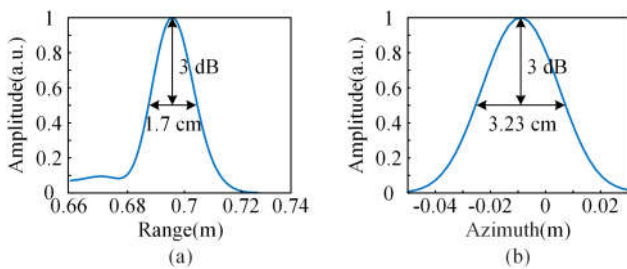

Fig. 14. (a) The range-resolved profile and (b) the azimuth-resolved profile of the brightest point in Fig. 13(d).

bandwidth, the ISAR image of the target becomes clearer, verifying that the dual-band fused microwave photonic radar system transmitting high-frequency and large-bandwidth LFM signals with arbitrary chirp rates has the capability of high-resolution target detection and imaging. In Fig. 14, the range-resolved profile and azimuth-resolved profile of the brightest point in Fig. 13(d) are given. The range resolution and azimuth resolution of each 3 dB lobe bandwidth are also marked. A hamming window is used in the process of radar imaging, thus the 3 dB
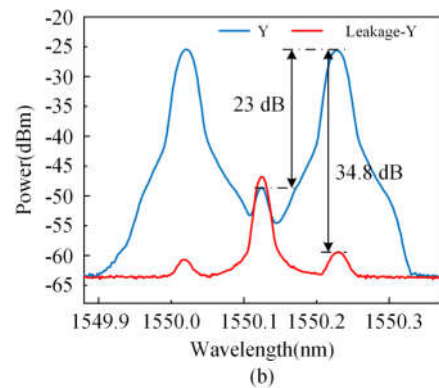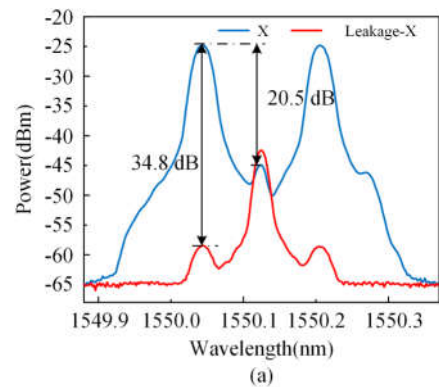

Fig. 15. Optical spectra of the signals along (a) the X polarization and (b) the Y polarization and their leakages.

bandwidth is expanded by a factor of 1.3 [32]. The theoretical range resolution is calculated according to the formula $1.3c/2B$, which is 1.65 cm. The experimentally measured value is 1.7 cm as can be seen in Fig. 13(a). The theoretical azimuth resolution is calculated according to the formula $1.3\lambda/2\Delta\theta$, in which λ is the center wavelength of the transmitted signal and $\Delta\theta$ is the accumulation angle used for imaging. The theoretical azimuth resolution is 3.1 cm while the experimentally measured value is 3.23 cm.

Dual polarization is used to distinguish signals of different bands, so only dual bands are supported in this paper. At last, we discuss the crosstalk between the two orthogonal polarizations. To do so, the LFM signal input to one of the MZMs in the Dpol-MZM is disconnected, and the corresponding output optical spectrum of the integrated 90° optical hybrid is detected by an optical spectrum analyzer (YOKOGAWA AQ6370C). From the optical spectra shown in Fig. 15(a) and (b), the power leakage between the orthogonally polarized reference signals can be measured. The rejection ratio has reached 34.8 dB. The crosstalk between the two polarizations is sufficiently weak to be ignored in the experiments. Moreover, the sideband carrier suppression ratio of the optical signal from the Dpol-MZM exceeds 20 dB, as illustrated in Fig. 15.

IV. CONCLUSION

In summary, a dual-band coherent microwave photonic radar realizing the generation and de-chirp processing of wideband

LFM signals with arbitrary chirp rates in two frequency bands is proposed. Based on the polarization multiplexing, the signals in the two frequency bands can be manipulated simultaneously with a compact structure. In addition, through the fusion of the dual-band LFM signals, the range resolution of the radar system is improved compared to the systems using only a single frequency band, enhancing the radar detection and imaging performance. An equivalent operating frequency range of 18.1–29.9 GHz is achieved by fusing the signals covering 18.1–23.1 GHz and 22.9–29.9 GHz. A range resolution of 1.31 cm is realized. The proposed radar also features a simple configuration, flexible operation, and good anti-jamming capability, which would provide a promising sensor for small UAV tracking, intelligent driving, and multi-target imaging.

REFERENCES

[1] C. Zhu, W. Hu, H. Zhu, and L. Li, "Research on radar development and application and signal processing technology," in *Proc. IEEE Int. Conf. Electron. Technol., Commun. Inf.*, 2021, pp. 130–134.

[2] F. Scotti, F. Laghezza, P. Ghelfi, and A. Bogoni, "Multi-band software-defined coherent radar based on a single photonic transceiver," *IEEE Trans. Microw. Theory Techn.*, vol. 63, no. 2, pp. 546–552, Feb. 2015.

[3] J. Shi et al., "Photonics-based dual-functional system for simultaneous high-resolution radar imaging and fast frequency measurement," *Opt. Lett.*, vol. 44, no. 8, pp. 1948–1951, Apr. 2019.

[4] X. Xu and J. Li, "Ultrawide-band radar imagery from multiple incoherent frequency subband measurements," *J. Syst. Eng. Electron.*, vol. 22, no. 3, pp. 398–404, Jun. 2011.

[5] C. Ma et al., "Microwave photonic imaging radar with a sub-centimeter-level resolution," *J. Lightw. Technol.*, vol. 38, no. 18, pp. 4948–4954, Sep. 2020.

[6] K. M. Cuomo, J. E. Pion, and J. T. Mayhan, "Ultrawide-band coherent processing," *IEEE Trans. Antennas Propag.*, vol. 47, no. 6, pp. 1094–1107, Jun. 1999.

[7] P. van Dorp, R. Ebeling, and A. G. Huizing, "High resolution radar imaging using coherent multiband processing techniques," in *Proc. IEEE Radar Conf.*, 2010, pp. 981–986.

[8] B. Hussain et al., "Performance analysis of auto-regressive UWB synthesis algorithm for coherent sparse multiband radars," in *Proc. Int. Conf. Radar Syst.*, 2017, pp. 1–6.

[9] J. Yao, "Photonic generation of microwave arbitrary waveforms," *Opt. Commun.*, vol. 284, no. 15, pp. 3723–3736, Jul. 2011.

[10] A. J. Seeds, "Microwave photonics," *IEEE Trans. Microw. Theory Techn.*, vol. 50, no. 3, pp. 877–887, Mar. 2002.

[11] J. Yao, "Microwave photonics," *J. Lightw. Technol.*, vol. 27, no. 3, pp. 314–335, Feb. 2009.

[12] J. Capmany and D. Novak, "Microwave photonics combines two worlds," *Nature Photon.*, vol. 1, no. 6, pp. 319–330, Jun. 2007.

[13] Q. Guo, F. Zhang, P. Zhou, and S. Pan, "Dual-band LFM signal generation by optical frequency quadrupling and polarization multiplexing," *IEEE Photon. Technol. Lett.*, vol. 29, no. 16, pp. 1320–1323, Aug. 2017.

[14] K. Zhang et al., "Photonic approach to dual-band dual-chirp microwave waveform generation with multiplying central frequency and bandwidth," *Opt. Commun.*, vol. 437, pp. 17–26, Apr. 2019.

[15] L. Wang et al., "Photonic generation and transmission of dual-band dual-chirp microwave waveforms at C-band and X-band with elimination of power fading," *IEEE Photon. J.*, vol. 13, no. 1, Feb. 2021, Art. no. 5500209.

[16] F. Yin, Z. Yin, X. Xie, Y. Dai, and K. Xu, "Broadband radio-frequency signal synthesis by photonic-assisted channelization," *Opt. Exp.*, vol. 29, no. 12, pp. 17839–17848, Jun. 2021.

[17] R. Zhu, M. Xu, Q. Liu, B. Wang, and W. Zhang, "Photonic generation of flexible ultra-wide linearly-chirped microwave waveforms," *Opt. Exp.*, vol. 29, no. 26, pp. 43731–43744, Dec. 2021.

[18] X. Zhang, Q. Sun, J. Yang, J. Cao, and W. Li, "Reconfigurable multi-band microwave photonic radar transmitter with a wide operating frequency range," *Opt. Exp.*, vol. 27, no. 24, pp. 34519–34529, Nov. 2019.

[19] H. Chen, B. Nakarmi, and S. Pan, "Multi-band LFM signal with unidentical bandwidths subjected to optical injection in a DFB laser," *IEEE Photon. Technol. Lett.*, vol. 33, no. 8, pp. 391–394, Apr. 2021.

[20] P. Ghelfi et al., "Photonics in radar systems: RF integration for state-of-the-art functionality," *IEEE Microw. Mag.*, vol. 16, no. 8, pp. 74–83, Sep. 2015.

[21] A. Wang et al., "Microwave photonic radar system with ultra-flexible frequency-domain tunability," *Opt. Exp.*, vol. 29, no. 9, pp. 13887–13898, Apr. 2021.

[22] P. Ghelfi, F. Laghezza, F. Scotti, D. Onori, and A. Bogoni, "Photonics for radars operating on multiple coherent bands," *J. Lightw. Technol.*, vol. 34, no. 2, pp. 500–507, Jan. 2016.

[23] T. H. Brandão et al., "Coherent dual-band radar system based on a unique antenna and a photonics-based transceiver," *Inst. Eng. Technol. Radar, Sonar Navigation*, vol. 13, no. 4, pp. 505–511, Apr. 2019.

[24] S. Peng et al., "A photonics-based coherent dual-band radar for super-resolution range profile," *IEEE Photon. J.*, vol. 11, no. 4, Aug. 2019, Art. no. 5502408.

[25] S. Wang et al., "Dual-band THz photonic pulses enabling synthetic mm-scale range resolution," *IEEE Photon. Technol. Lett.*, vol. 30, no. 20, pp. 1760–1763, Oct. 2018.

[26] J. Cao et al., "Photonic deramp receiver for dual-band LFM-CW Radar," *J. Lightw. Technol.*, vol. 37, no. 10, pp. 2403–2408, May 2019.

[27] Z. Meng et al., "Dual-band dechirping LFMCW radar receiver with high image rejection using microwave photonic I/Q mixer," *Opt. Exp.*, vol. 25, no. 18, pp. 22055–22065, Sep. 2017.

[28] F. Cao et al., "Dual-band high range-resolution microwave photonic radar based on coherent fusion processing," in *Proc. IEEE Comput. Ind. Eng. Int. Conf. Radar*, 2021, pp. 3137–3140.

[29] W. Zou et al., "Rational sampling rate transformation for wideband signals," *Dianxun Jishu/Telecommun. Eng.*, vol. 52, no. 11, pp. 1783–1786, 2012.

[30] H. Maître, "The principles of synthetic aperture radar," in *Processing of Synthetic Aperture Radar Images*, Hoboken, NJ, USA: Wiley, 2008, pp. 25–55.

[31] V. C. Chen and M. Martorella, *Inverse Synthetic Aperture Radar Imaging: Principles, Algorithms and Applications*. Herts, U.K.: SciTech, 2014.

[32] F. J. Harris, "On the use of windows for harmonic analysis with the discrete Fourier transform," *Proc. IEEE*, vol. 66, no. 1, pp. 51–83, Jan. 1978.

Xiangchuan Wang received the B.Eng. degree in automation and the Ph.D. degree in microelectronics and solid-state electronics from Nanjing University, Nanjing, China, in 2009 and 2015, respectively. He is currently a Research Professor with the Key Laboratory of Radar Imaging and Microwave Photonics, Ministry of Education, Nanjing University of Aeronautics and Astronautics, Nanjing. His research interests include microwave photonics measurement and radar imaging.

Fengting Cao received the B.S. degree from Jiangnan University, Wuxi, China, in 2020. She is currently working toward the M.S. degree with the Key Laboratory of Radar Imaging and Microwave Photonics, Ministry of Education. Her research focuses on microwave photonic radar.

Cong Ma received the B.S. degree from the Civil Aviation University of China, Tianjin, China, in 2016, and the M.S. degree in 2021 from the Nanjing University of Aeronautics and Astronautics, Nanjing, China, where he is currently working toward the Ph.D. degree with the Key Laboratory of Radar Imaging and Microwave Photonics, Ministry of Education. His research focuses on microwave photonic radars for high-resolution imaging.

Yue Yang received the B.S. degree in 2018 from the Nanjing University of Aeronautics and Astronautics, Nanjing, China, where he is currently working toward the Ph.D. degree with the Key Laboratory of Radar Imaging and Microwave Photonics, Ministry of Education. His main research interests include photonics-based radars for high-resolution imaging and photonics-based array detection.

Fangzheng Zhang (Senior Member, IEEE) received the B.S. degree from the Huazhong University of Science and Technology, Wuhan, China, in 2008, and the Ph.D. degree from the Beijing University of Posts and Telecommunications, Beijing, China, in 2013. He is currently a Full Professor with the College of Electronic and Information Engineering, Nanjing University of Aeronautics and Astronautics, Nanjing, China. His main research interests include microwave photonics, radar imaging, and machine learning.

Shilong Pan (Fellow, IEEE) received the B.S. and Ph.D. degrees in electronic engineering from Tsinghua University, Beijing, China, in 2004 and 2008, respectively. From 2008 to 2010, he was a "Vision 2010" Postdoctoral Research Fellow with the Microwave Photonics Research Laboratory, University of Ottawa, Ottawa, ON, Canada. In 2010, he joined the College of Electronic and Information Engineering, Nanjing University of Aeronautics and Astronautics, Nanjing, China, where he is currently a Full Professor and the Director of the National Key Laboratory of Microwave Photonics.

His research focuses on microwave photonics, which include optical generation and processing of microwave signals, analog photonic links, photonic microwave measurement, and integrated microwave photonics.

Dr. Pan is currently the Deputy Editor of *Chinese Optics Letters*, an Associate Editor for the IEEE/Optica Journal of Lightwave Technology, IEEE Transactions on Microwave Theory and Techniques, and *Electronics Letters*, and is the Vice Chair of IEEE MTT-22 Microwave Photonics. He was the Chair of a number of international conferences, symposia, and workshops, including the TPC Chair of the ICOCN 2015, TPC Chair of IEEE MWP in 2023, TPC Co-Chair of IEEE MWP 2017, and General Co-Chair of IEEE MWP 2021.

Dr. Pan is a Fellow of Optica, SPIE, and IET. He was selected as an IEEE Photonics Society Distinguished Lecturer in 2019 and an IEEE MTT-S Distinguished Microwave Lecturer in 2022. He was the recipient of the IEEE MTT-S Outstanding Young Engineer Award in 2021.